Effect of pH on Phase, Morphology and Photocatalytic Properties of BiOBr Synthesized by Hydrothermal Method

Prakasit Intaphong[1] · Anukorn Phuruangrat[1] ⬤ · K. Karthik[2] · Phattranit Dumrongrojthanath[3] · Titipun Thongtem[4,5] · Somchai Thongtem[4,6]

Abstract

Effect of pH on crystalline structure, morphology and visible-light-driven photocatalysis of BiOBr samples hydrothermally synthesized in solutions with the pH of 2–10 was investigated. The as-synthesized BiOBr samples investigated by X-ray diffraction, Raman spectroscopy, Fourier transform infrared spectroscopy, scanning electron microscopy, transmission electron microscopy and X-ray photoelectron spectroscopy. In this research, the as-synthesized samples are pure tetragonal BiOBr phase at the pH of 2–10, and were composed of microplates, nanoplates and hierarchical micro-flowers controlled by the solution pH. The as-synthesized sample at the pH 8 was revealed the presence of Bi 4f, O 1s and Br 3d. Visible-light-driven photocatalytic properties of the BiOBr photocatalyst with different morphologies were investigated through the photodegradation of rhodamine B (RhB). The BiOBr hierarchical micro-flowers synthesized in the solution with the pH 8 show the best photocatalytic activity for wastewater treatment and the $^{\cdot}O_2^{\,-}$ radicals were attributed to be the primary active species for photodegradation of RhB under visible light irradiation.

Keywords BiOBr hierarchical micro-flowers · Photocatalysis · Spectroscopy

✉ Anukorn Phuruangrat
phuruangrat@hotmail.com

✉ Somchai Thongtem
schthongtem@yahoo.com

1 Department of Materials Science and Technology, Faculty of Science, Prince of Songkla University, Hat Yai, Songkhla 90112, Thailand

2 Department of Physics, Bharathidasan University, Tiruchirappalli, Tamil Nadu 620 024, India

3 Rajamangala University of Technology Lanna Chiang Rai, Chiang Rai 57120, Thailand

4 Materials Science Research Center, Faculty of Science, Chiang Mai University, Chiang Mai 50200, Thailand

5 Department of Chemistry, Faculty of Science, Chiang Mai University, Chiang Mai 50200, Thailand

6 Department of Physics and Materials Science, Faculty of Science, Chiang Mai University, Chiang Mai 50200, Thailand

1 Introduction

The semiconductor photocatalysis as green technology is widely used for the degradation of harmful waste products such as dyes, insecticides, pesticides and toxic organic pollutants in wastewater to CO_2, H_2O and other small molecules at room temperature, including for splitting of water and production of hydrogen under light irradiation [1–5]. The widely used TiO_2 photocatalyst is active only under UV light irradiation (5% of solar radiation) because its band gap is 3.20 eV [2, 3, 6, 7]. Thus a number of researchers have done the research on visible-light-driven semiconductor photocatalysts [2, 3, 8]. Visible-light-driven bismuth based semiconductors such as $BiVO_4$ [1, 2], Bi_2MoO_6 [3, 9], Bi_2WO_6 [10–12], BiOX (X = Br, Cl and I) [13–18] are attractively interesting for wastewater treatment. Among them, bismuth oxide bromide (BiOBr) as ternary semiconductor materials with layered structure has an appropriate band gap of about 2.75 eV because it responds to visible-light and has outstanding chemical stability, leading it to be a promising visible-light-driven photocatalytic candidate [19–21]. BiOBr as layered structure is built up by strong electrovalent bond between $[Bi_2O_2]^{2+}$ slab embedded in double slabs

of Br⁻ along the [001] direction, while two closely adjacent slabs of Br⁻ are connected by van der Waals force of attraction. These lead to the formation of induced dipole and effective separation of photon-induced electrons and holes, enhancing the photocatalytic activity for degradation of harmful waste products [13, 20–22]. There are many methods used to synthesize BiOBr nanostructure such as solvothermal method [13, 21], anodization [15], hydrothermal method [20], combustion method [23] and microwave-assisted hydrothermal method [24] with different morphologies such as hierarchical microspheres [13, 25], nanosheets [15, 20, 22, 23] and hollow microspheres [21, 24]. Among them, hydrothermal method is more advantage than other methods because it requires low temperature synthesis and is one step synthesis with no sintering and calcination. It is low cost process and is able to control shape, size and phase, including the requirement of mild condition and less energy consumption [26–29]. Thus the hydrothermal method was used to synthesize porous hierarchical BiOBr micro-flowers by controlling pH of the precursor solution because the flowers have higher surface area for absorbing visible light and dyes in aqueous solution, and enhancing photocatalytic activity for degradation of organic dye in wastewater [16, 17].

In this work, the influence of pH (acidity/basicity scale) on crystalline structure, morphology and visible-light-driven photocatalytic properties of as-obtained BiOBr samples synthesized by a simple hydrothermal method was studied. This method was used to synthesize BiOBr hierarchical micro-flowers with high surface area without template adding. The visible-light-driven photocatalytic activities of as-prepared BiOBr samples in the solutions with different pH were evaluated through the decomposition of rhodamine B (RhB) solution. The BiOBr hierarchical micro-flowers showed very good visible-light-driven photocatalytic activity for degradation of RhB solution.

2 Experiment

Each 0.005 mmol Bi(NO₃)₃·5H₂O was dissolved in each of 75 ml reverse osmosis water under stirring. Subsequently, 0.005 mmol NaBr was dissolved in each of these solutions with continued stirring for 30 min. The solution pH was adjusted to 2, 4, 6, 8, 10 and 12 by 1 M HCl and 3 M NaOH solutions. These solutions were transferred to 200 ml Teflon-lined stainless steel autoclaves. The autoclaves were heated at 180 °C for 20 h in an electric oven. In the end, the as-formed white precipitates were filtered, washed with deionized water and ethanol to remove the residual ions such as Na⁺ and NO₃⁻, and dried for further characterization. The BiOBr photocatalysts were labeled as BiOBr-2, BiOBr-4, BiOBr-6, BiOBr-8, BiOBr-10 and BiOBr-12 for the pH of the synthetic solutions of 2, 4, 6, 8, 10 and 12, respectively.

Phase of products was investigated by an X-ray diffractometer (XRD, Philips X'Pert MPD) with Cu K$_\alpha$ as an X-ray source operating at 20 kV and 15 mA in the 2θ range of 10°–60°, including the morphology by a field emission scanning electron microscope (FE-SEM, JEOL JSM-6335F) operating at 35 kV. Transmission electron microscopic images and selected area electron diffraction (SAED) pattern were operated through a transmission electron microscope (TEM, JEOL JEM-2010) operating at 200 kV. A Fourier transform infrared (FTIR) spectrometer was carried on a Bruker Tensor 27 spectrometer with KBr as a diluting reagent. A Raman spectrophotometer was recorded on a T64000 HORIBA Jobin-Yvon spectrometer using Ar green laser at 514.5 nm wavelength. An X-ray photoelectron spectrometer (XPS, Axis Ultra DLD, Kratos Analytical Ltd spectrometer) was carried out using Al K$_\alpha$ at 1486.6 eV as an excitation source and C 1s at 285.1 eV as a standard. Brunauer–Emmett–Teller (BET) surface area was studied for nitrogen adsorption by a Quantachrome Autosorb-1-C analyzer at 77 K.

Photocatalytic activity was evaluated through the degradation of rhodamine B (RhB) as a model dye solution. The 0.2 g photocatalyst was added to 1×10^{-5} M of 200 ml RhB solution which was magnetically stirred in the dark for 30 min to form homogeneous solution and to achieve adsorption–desorption equilibrium. Photocatalysis was proceeding under a visible light radiation (λ ≥ 420 nm) of Xe lamp without a filter. During photocatalysis, 5 ml (approx.) RhB solution was withdrawn every 15 min and centrifuged. The content of RhB in the solution was measured by a UV–visible spectrophotometer at λ$_{max}$ of 554 nm. The residual content of RhB was calculated using the equation.

$$\text{Decolorization efficiency}(\%) = \frac{C_o - C_t}{C_o} \times 100 \qquad (1)$$

where C_o is the initial concentration of RhB at adsorption–desorption equilibrium and C_t is the concentration of RhB after visible light irradiation within the elapsed time (t). In the end, the degraded RhB solution were studied by direct mass spectrometry (MS) using a positive electrospray ionization (ESI⁺) mode.

3 Results and Discussion

Phase of the samples synthesized at different pH was investigated by XRD analysis. The XRD patterns of all the as-synthesized BiOBr samples are shown in Fig. 1. The samples from BiOBr-2 to BiOBr-10 show the diffraction peaks at 2θ of 11.00°, 22.03°, 25.23°, 31.78°, 32.25°, 39.36°, 46.26°,
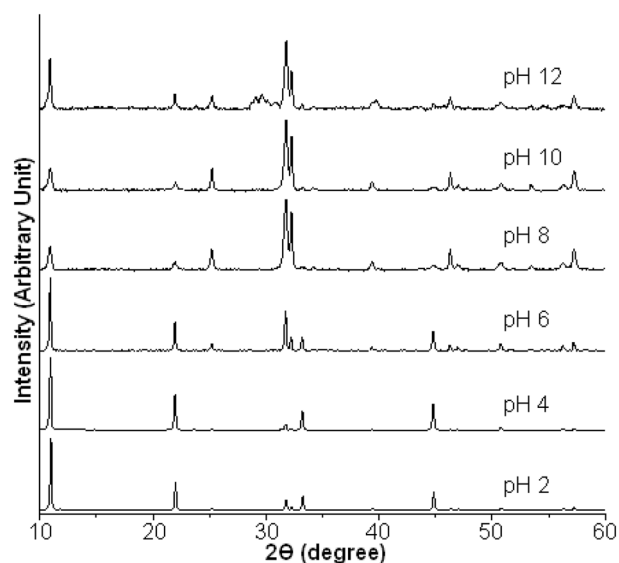
Fig. 1 XRD patterns of the samples synthesized in the solutions with different pH by hydrothermal method

50.75°, 53.38°, 56.26°, and 57.26° which can be indexed to the (001), (002), (101), (102), (110), (112), (200), (104), (211), (114) and (212) planes of pure tetragonal BiOBr, respectively, in agreement to the JCPDS no. 78-0348 [30]. The XRD patterns of all as-prepared samples show intense and sharp diffraction peaks, suggesting that all the samples were well crystallized in nature. They should be noted for the BiOBr sample synthesized in high acidic condition that the (001), (002) and (003) planes are higher than that of the (110) plane, implying that the (001) facet of the sample tended to be more exposed with the medium solution and eventually generated the sheet structure [23, 31, 32]. Moreover, the intensity of the (110) crystalline face of the BiOBr samples synthesized in acidic condition is weaker than that of the BiOBr samples synthesized in basic condition, suggesting that the (110) facet of the as-synthesized BiOBr-8 and BiOBr-10 samples are preferred growth orientation [20]. For the BiOBr-12 sample, mixed phases of bismuth oxide bromide as monoclinic $Bi_4O_5Br_2$ (JCPDS no. 37-0699 [30]), orthorhombic Bi_3O_4Br (JCPDS no. 37-0700 [30]) and tetragonal BiOBr (JCPDS no. 78-0348 [30]) were detected.

FTIR and Raman spectra of the as-synthesized samples from BiOBr-2 to BiOBr-10 are shown in Fig. 2. The FTIR spectra of these samples appear as the sharp and weak absorption bands at 512 cm^{-1} and 770 cm^{-1} which correspond to the stretching vibration of Bi–O bond [19, 24, 32, 33]. Raman spectra of the as-synthesized samples from BiOBr-2 to BiOBr-10 show strong peaks at 57.8 cm^{-1} and 113.14 cm^{-1} which are assigned to external and internal A_{1g} of Bi–Br stretching mode [19, 24, 32]. Raman peak at 91.0 cm^{-1} is assumed to be the Bi–Br stretching mode [19, 24, 32]. The Raman peak at 160.5 cm^{-1} is in accordance
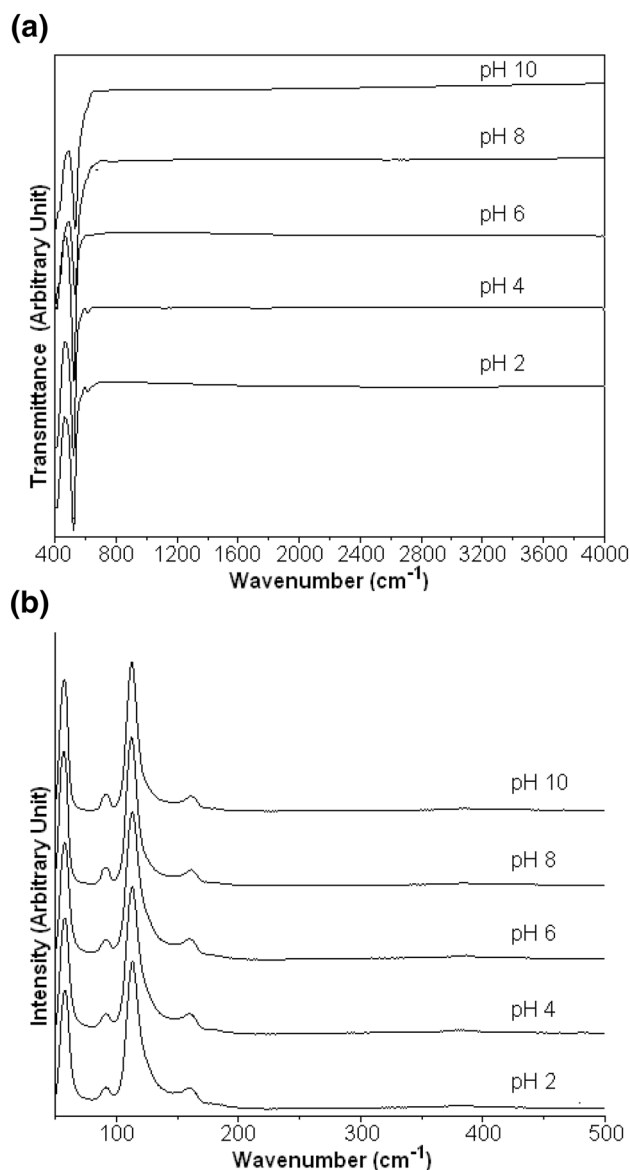

Fig. 2 **a** FTIR and **b** Raman spectra of BiOBr samples synthesized in the solutions with different pH by hydrothermal method

with the E_g internal Bi–Br stretching mode while the weak peak at 382.3 cm^{-1} is assigned to the E_g and B_{1g} peaks generated by the motion of oxygen atoms, in accordance with the previous reports [19, 24, 32].

XPS analysis was conducted to investigate chemical state and elemental composition of BiOBr sample. The XPS survey (Fig. 3a) shows that BiOBr-8 contains major elements of Bi, O and Br. Figure 3b shows two peaks of Bi 4f at binding energies of 159.72 eV and 165.03 eV corresponding to the Bi $4f_{7/2}$ and Bi $4f_{5/2}$, respectively. The analysis suggested that Bi species containing in BiOBr is trivalent oxidation state [3, 9, 20, 31, 32]. Figure 3c resolved the XPS spectrum of O 1s peak located at 530.54 eV which can be identified to the

Fig. 3 XPS spectra of BiOBr sample synthesized in the solution with the pH 8: **a** survey, **b** Bi 4f, **c** O 1s and **d** Br 3d
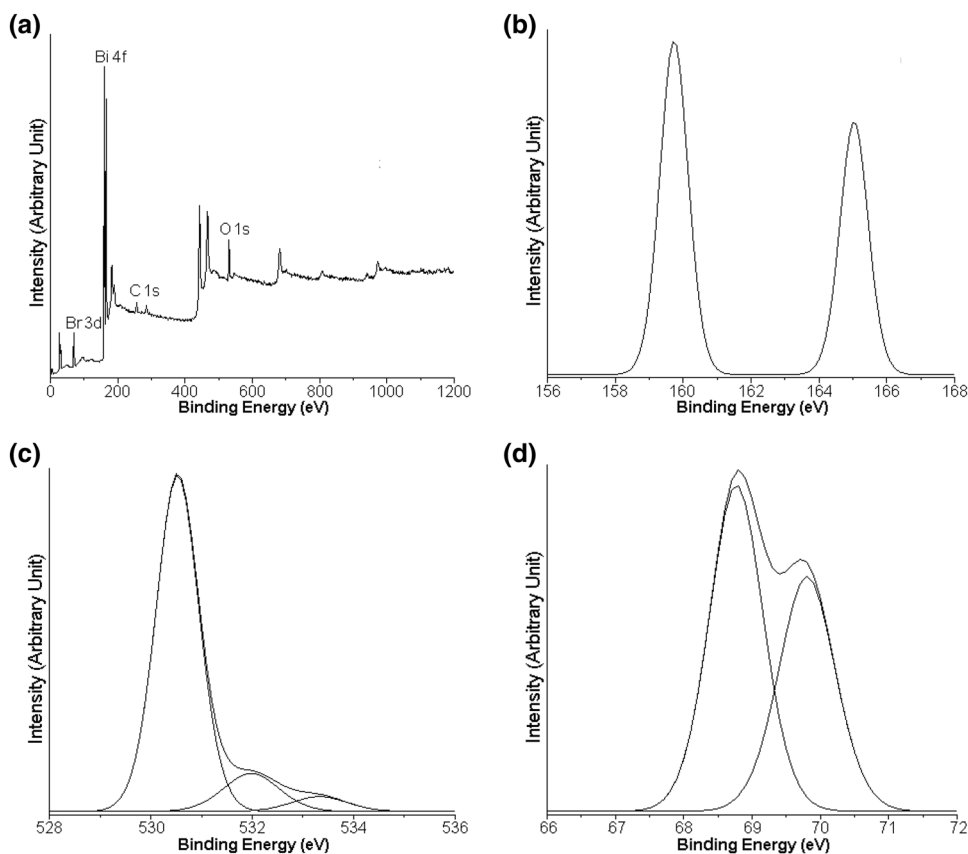
oxygen lattice in the $(BiO)_2^{2+}$ slabs of the BiOBr sample. The three Gaussian peaks of O 1 s at 530.50 eV, 531.58 eV and 533.27 eV are attributed to the Bi–O bond in BiOBr lattice and surface O–H and C–O groups adsorbed on the surface of BiOBr [3, 9, 13, 20, 32]. Those of Br $3d_{5/2}$ and Br $3d_{3/2}$ core levels (Fig. 3d) were detected at the binding energies of 68.78 eV and 69.80 eV, which are attributed to Br^- in BiOBr lattice [20, 31, 32].

Figure 4 shows SEM images of the BiOBr samples synthesized in the solutions with different pH, and revealed the evolution of product morphologies. Clearly, the morphologies of as-synthesized BiOBr samples were controlled by the pH of precursor solutions. The BiOBr-2 sample was composed of microplates which were developed to mixed microplates and nanoplates containing in BiOBr-4. Subsequently, the nanoplates were self-assemble by forming porous hierarchical micro-flowers in BiOBr-8 sample. In the end, the petals of hierarchical micro-flowers grew and broke into thin nanosheets in BiOBr-10.

The morphologies of the as-synthesized samples were characterized by TEM as the results shown in Fig. 5. Clearly, the BiOBr-2 sample was composed of smooth microplates with size of 2–4 μm. The size of microplates was decreased to 400–600 nm for BiOBr-4. Then, self-assembling character of nanoplates to form micro-flowers at the pH 6 was detected. At the pH 8, the BiOBr-8

presented porous structure made up of uniform hierarchical micro-flowers of packing nanoplates. At high magnification, these hierarchical micro-flowers were assembled by interweaving nanoplates with each other to produce a large amount of mesopores. According to the previous reports, the hierarchical micro-flowers are favorable for uniform adsorption of RhB on surface of BiOBr hierarchical micro-flowers and enhanced photocatalytic degradation of RhB solution [1, 14, 21]. The selected area electron diffraction of BiOBr-8 shows spots of electron diffraction which were indexed to the (− 102), (004) and (102) planes with an angle of 45.9°, indicating the BiOBr-8 nanoplates with the (010) exposed facets on the top and bottom surfaces [32]. At the pH 10, the petals of BiOBr hierarchical micro-flowers grew and broke to thin nanosheets.

Figure 6 shows the UV–visible spectra of BiOBr in wavelength range of 200–800 nm indicating that all samples have excellent absorption in UV–visible range due to the band-gap transition [34–36]. They should be noted that UV–visible of BiOBr shows a broad UV–visible band caused by the generation of defects and local bond distortion such as surface oxygen vacancies, intrinsic surface states and confined electronic level within the forbidden band gap [37, 38]. Clearly, BiOBr is a promising photocatalyst under visible-light irradiation.
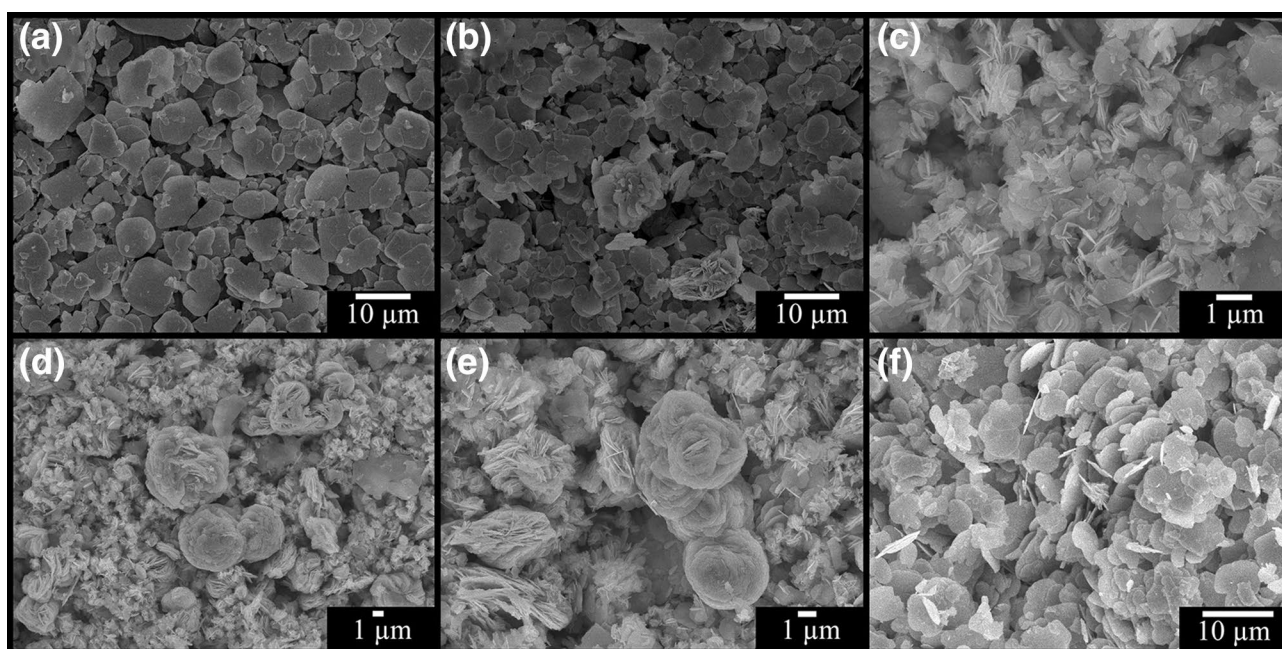
Fig. 4 SEM images of BiOBr samples synthesized in the solutions with the pH: **a** 2, **b** 4, **c** 6, **d**, **e** 8 and **f** 10
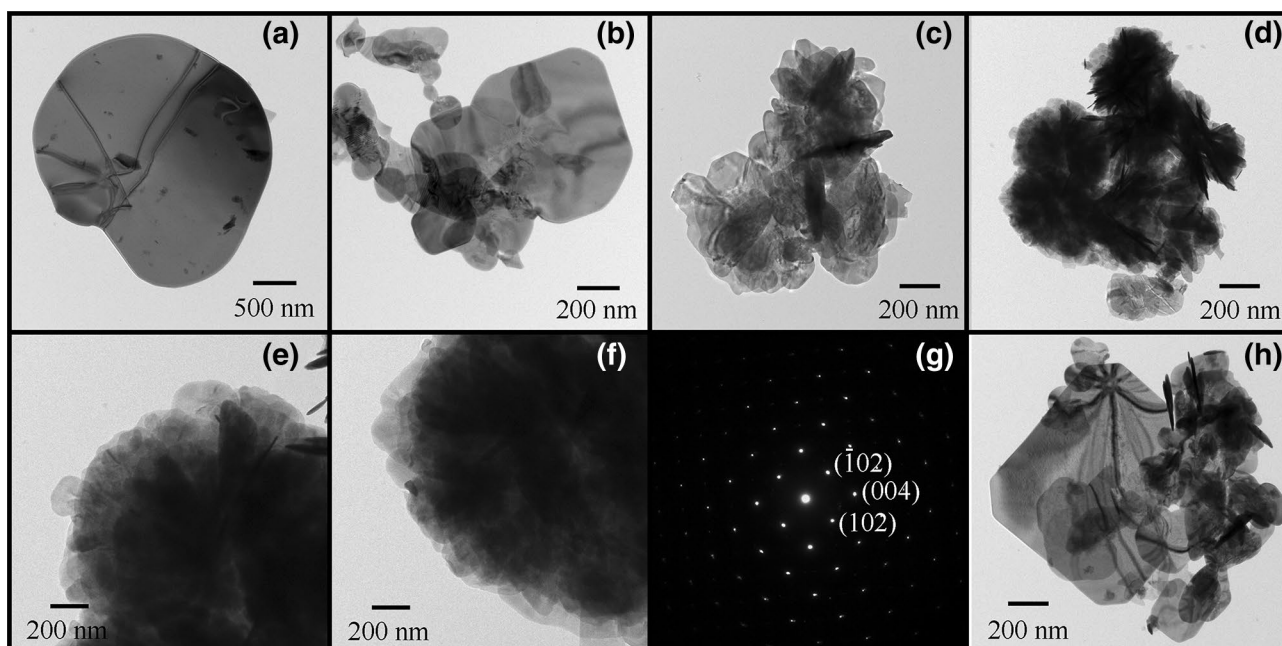

Fig. 5 TEM images and SAED pattern of BiOBr samples synthesized in the solutions with the pH: **a** 2, **b** 4, **c** 6, **d**, **e**, **g** 8 and **f**, **h** 10

Figure 7a shows absorption spectra of the RhB solution photocatalyzed by BiOBr-8 at 554 nm as a function of visible-light irradiation. Upon increasing of irradiation time, the absorption peak of RhB decreased and showed blue-shift to lower wavelength due to de-ethylation of RhB during the photodegradation process [3, 25, 39, 40]. At the end of 45 min irradiation, the pink color of RhB aqueous solution changed to colorless, suggesting that RhB molecules were completely decomposed. The photocatalytic degradation of RhB under visible light irradiation ($\lambda \geq 420$ nm) by BiOBr samples synthesized at different pH is shown in Fig. 7b. Among the as-synthesized photocatalysts, the degradation rates decreased in sequence as follows: BiOBr-8 > BiOBr-6 > BiOBr-4 > BiOBr-10 > BiOBr-2. The photodegradation efficiency of RhB
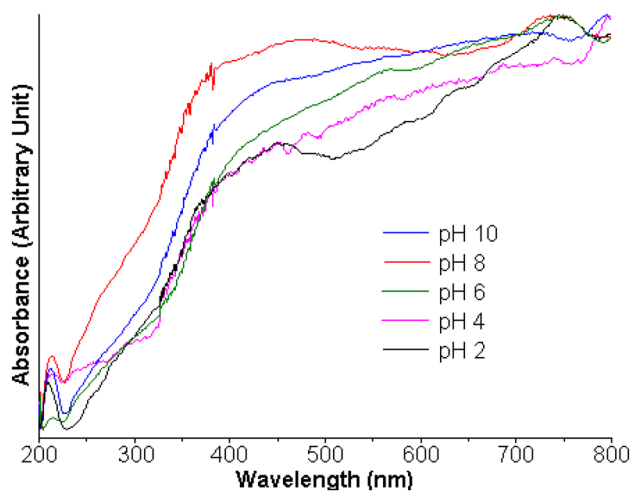
Fig. 6 UV–visible spectra of BiOBr samples synthesized in the solutions with different pH by hydrothermal method in the wavelength range of 200–800 nm

by BiOBr-8 was the highest at 99%. Similarly, for the BET analysis, their surface areas were 12.9770 $m^2 g^{-1}$ (BiOBr-8) > 8.8753 $m^2 g^{-1}$ (BiOBr-6) > 5.3584 $m^2 g^{-1}$ (BiOBr-4) > 3.5681 $m^2 g^{-1}$ (BiOBr-10) > 3.0536 $m^2 g^{-1}$ (BiOBr-2). BiOBr-8 shows the highest photocatalytic activity because it has the largest surface area for the photocatalytic process. The photocatalytic reaction follows the apparent first-order kinetic model [11, 19, 33]. Figure 7c shows the plot of ln (C_o/C_t) versus irradiation time for photodegradation of RhB by BiOBr synthesized at different pH and the data were fitted to a linear line [11, 39, 40]. The pseudo first-order rates for photodegradation of RhB under visible light irradiation are 0.0352, 0.0555, 0.0665, 0.0995 and 0.0502 min^{-1} for BiOBr-2, BiOBr-4, BiOBr-6, BiOBr-8 and BiOBr-10, respectively. The reaction rate constant significantly increased with the pH of solution increased from the pH 2 to 8 because of the increasing in surface area and active surface sites of BiOBr samples from BiOBr-2 to BiOBr-8. The reaction rate was reduced when the pH for the synthetic process was 10. The stability of BiOBr-8 photocatalyst was investigated by monitoring the re-used photocatalyst for five cycles as the results shown in Fig. 7d. Clearly, photodegradation efficiency of BiOBr-8 decreased
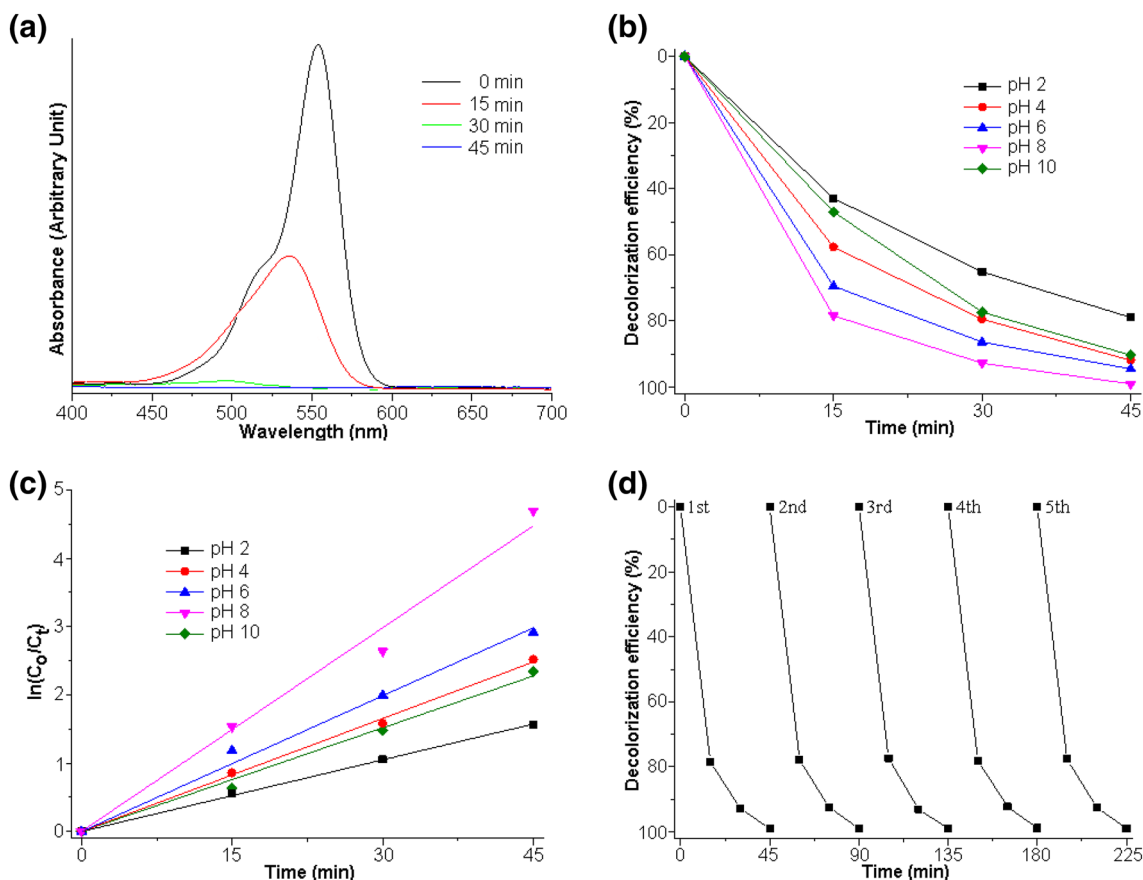

Fig. 7 **a** UV–visible spectra of RhB after being photodegraded by BiOBr-8 under visible light irradiation. **b** Decolorization efficiency and **c** pseudo first-order plot for photodegradation of RhB by BiOBr samples synthesized in the solutions with different pH under visible light irradiation. **d** Decolorization efficiency of the reused BiOBr-8 photocatalyst for five cycles
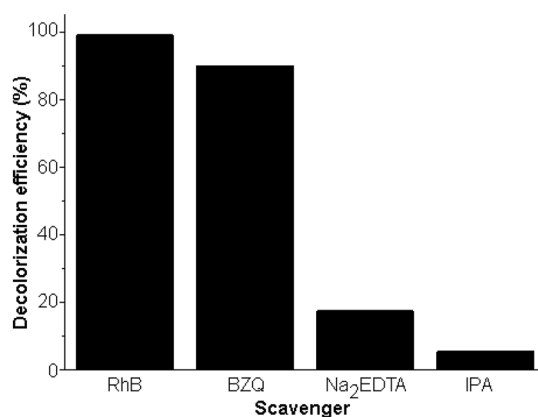
Fig. 8 Bar chart of different dyes after being photodegraded by BiOBr sample synthesized in the solution with the pH 8

Fig. 9 Mass spectra of RhB: **a** at adsorption–desorption equilibrium and **b** after being photodegraded by BiOBr-8 under visible light within 45 min

slightly within five cycles of photocatalytic test. Thus the BiOBr-8 is stable and can be reused for several cycles for degradation of RhB under visible light irradiation.

The main active species for photocatalytic degradation of different dyes by the as-synthesized BiOBr sample under visible light irradiation were studied as the results shown in Fig. 8. Different agents as p-benzoquinone (BZQ, linear formula $C_6H_4(=O)_2$) for superoxide radical ($^{\cdot}O_2{}^{-}$) scavenger, disodium ethylenediaminetetraacetate (Na_2EDTA) for hole (h^+) scavenger and isopropyl alcohol (IPA) for hydroxyl radical ($^{\cdot}OH$) scavenger were also tested for photocatalysis [41–43]. In this research, the photodegradation efficiencies of BZQ, Na_2EDTA and IPA by BiOBr-8 under visible light irradiation within 45 min were 90.21%, 17.38% and 5.38%, respectively. The $^{\cdot}O_2{}^{-}$ radicals were attributed to be the primary active species for photodegradation of RhB by BiOBr-8 under visible light irradiation.

Figure 9 shows the analytical results for the direct mass spectrometry that ionizes chemical species and identifies ions into spectra based on the mass to charge ratio. These results were the species at the adsorption–desorption equilibrium and the remaining species after photodegradation of RhB by BiOBr-8 within 45 min under visible light irradiation. The direct mass spectrum shows the m/z ratio of RhB at the adsorption–desorption equilibrium at 443 [44–46]. When the photocatalysis was proceeding for 45 min, the mass to charge ratio of RhB at 443 was not detected in the mass spectrum. The analytical spectrum certified that the RhB molecules were photodegraded by super oxide anion radicals under visible light irradiation.
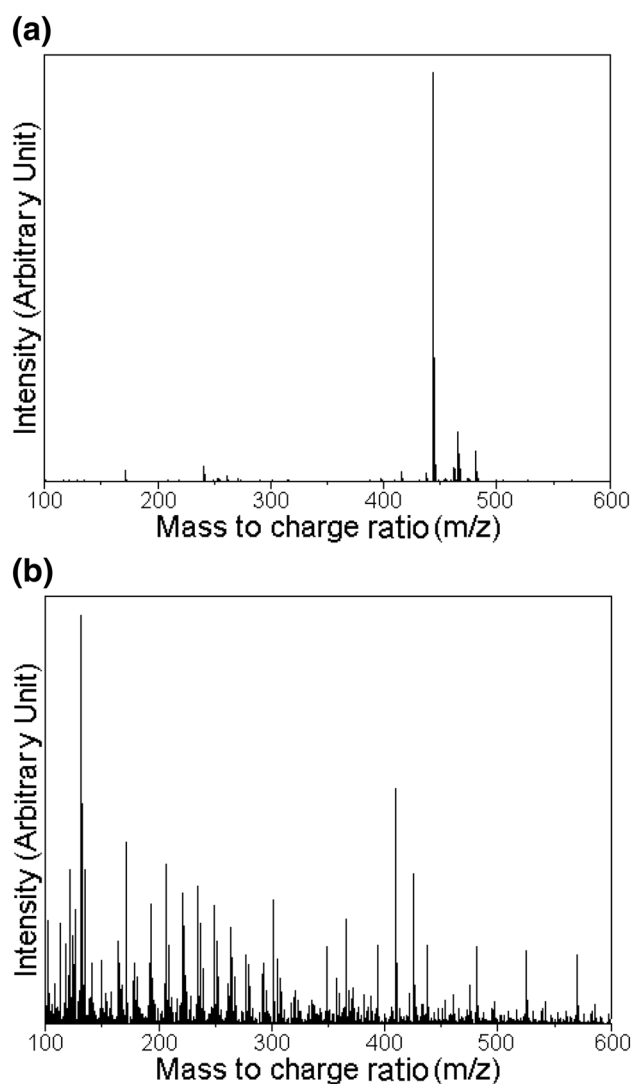
4 Conclusions

The visible-light driven BiOBr photocatalysts were successfully synthesized by hydrothermal method in the solutions with the pH of 2–10. The BiOBr samples show pure tetragonal BiOBr phase with different morphologies controlled by the solution pH. In this research, BiOBr-8 sample was composed of uniform hierarchical micro-flowers of assembling nanoplates which are favorable for uniform adsorption of RhB on the surface of BiOBr hierarchical micro-flowers for photodegradation of RhB molecules. The as-synthesized BiOBr-8 sample as the highest photocatalytic activity and the promising stability can be considered as a visible-light-driven photocatalyst for wastewater treatment.

References

1. F. Li, C. Yang, Q. Li, W. Cao, T. Li, Mater. Lett. **145**, 52 (2015)
2. Z. Zhang, W. Wang, M. Shang, W. Yin, Catal. Commun. **11**(11), 982 (2010)
3. J. Bi, L. Wu, J. Li, Z. Li, X. Wang, X. Fu, Acta Mater. **55**(14), 4699 (2007)
4. Z. Shao, T. Zeng, Y. He, D. Zhang, X. Pu, Chem. Eng. J. **359**, 485 (2019)
5. Y. Tang, X. Li, D. Zhang, X. Pu, B. Ge, Y. Huang, Mater. Res. Bull. **110**, 214 (2019)
6. S. Liang, T. Zhang, D. Zhang, X. Pu, X. Shao, W. Li, J. Dou, J. Am. Ceram. Soc. **101**(8), 3424 (2018)
7. C. Yu, W. Zhou, L. Zhu, G. Li, K. Yang, R. Jin, Appl. Catal. B **184**, 1 (2016)
8. D. Zeng, K. Yang, C. Yu, F. Chen, X.X. Li, Z. Wu, H. Liu, Appl. Catal. B **237**, 449 (2018)
9. S. Jonjana, A. Phuruangrat, T. Thongtem, S. Thongtem, Mater. Lett. **172**, 11 (2016)
10. J. Li, Z. Liang, L. Guo, N. Lei, Q. Song, Mater. Lett. **223**, 93 (2018)
11. M.H. Selvi, P.R. Vang, M. Ashok, Optik **173**, 227 (2018)
12. S. Jonjana, A. Phuruangrat, T. Thongtem, B. Kuntalue, S. Thongtem, Mater. Lett. **218**, 146 (2018)
13. X. Meng, Z. Zhang, Mater. Lett. **225**, 152 (2018)
14. J.C. Ahern, R. Fairchild, J.S. Thomas, J. Carr, H.H. Patterson, Appl. Catal. B **179**, 229 (2015)
15. J. Zhao, X. Lv, X. Wang, J. Yang, X. Yang, X. Lu, Mater. Lett. **158**, 40 (2015)
16. M. Gao, J. Yang, T. Sun, Z. Zhang, D. Zhang, H. Huang, H. Lin, Y. Fang, X. Wang, Appl. Catal. B **243**, 734 (2019)
17. W. Fang, C. Yu, J. Mater. Res. **30**(20), 3125 (2015)
18. C. Yu, F. Cao, G. Li, R. Wei, J.C. Yu, R. Jin, Q. Fan, C. Wang, Sep. Purif. Technol. **120**, 110 (2013)
19. M. Ji, Z. Zhang, J. Xia, J. Di, Y. Liu, R. Chen, S. Yin, S. Zhang, H. Li, Chin. Chem. Lett. **29**(6), 805 (2018)
20. D. Wu, S. Yue, W. Wang, T. An, G. Li, L. Ye, H.Y. Yip, P.K. Wong, Appl. Surf. Sci. **391**, 516 (2017)
21. H.T. Wang, M.S. Shi, H.F. Yang, N. Chang, H. Zhang, Y.P. Liu, M.C. Lu, D. Ao, D.Q. Chu, Mater. Lett. **222**, 164 (2018)
22. H. Feng, Z. Xu, L. Wang, Y. Yu, D. Mitchell, D. Cui, X. Xu, J. Shi, T. Sannomiya, Y. Du, W. Hao, S.X. Dou, A.C.S. Appl, Mater. Interfaces **7**(50), 27592 (2015)
23. M. Gao, D. Zhang, X. Pu, H. Li, J. Li, X. Shao, K. Ding, Mater. Lett. **140**, 31 (2015)
24. Z. Chen, J. Zeng, J. Di, D. Zhao, M. Ji, J. Xia, H. Li, Green Energy Environ. **2**(2), 124 (2017)
25. L. Lin, M. Huang, L. Long, D. Chen, J. Alloy Compd. **615**, 929 (2014)
26. Y. Köseoğlu, F. Alan, M. Tan, R. Yilgin, M. Öztürk, Ceram. Int. **38**, 3625 (2012)
27. A. Phuruangrat, D.J. Ham, S.J. Hong, S. Thongtem, J.S. Lee, J. Mater. Chem. **20**, 1683 (2010)
28. Q. Liang, F. Qiao, X. Cui, X. Hou, Mater. Sci. Semicond. Process. **89**, 154 (2019)
29. H.A.J.L. Mourão, O.F. Lopes, C. Ribeiro, V.R. Mastelaro, Mater. Sci. Semicond. Process. **30**, 651 (2015)
30. Powder Diffract. File, JCPDS Internat. Centre Diffract. Data, PA 19073–3273, U.S.A. (2001)
31. D. Wu, S. Yue, W. Wang, T. An, G. Li, H.Y. Yip, H. Zhao, P.K. Wong, Appl. Catal. B **192**, 35 (2016)
32. L. Lu, M.Y. Zhou, L. Yin, G.W. Zhou, T. Jiang, X.K. Wan, H.X. Shi, J. Mol. Catal. A **423**, 379 (2016)
33. O. Mehraj, N.A. Mir, B.M. Pirzada, S. Sabir, Appl. Surf. Sci. **332**, 419 (2015)
34. Z. Wei, R. Li, R. Wang, RSC Adv. **8**(15), 7956 (2018)
35. Q.L. Yuan, Y. Zhang, H.Y. Yin, Q.L. Nie, W.W. Wu, J. Exp. Nanosci. **11**(5), 359 (2016)
36. D. Wu, S. Yue, W. Wang, T. An, G. Li, H.Y. Yip, H. Zhao, P.K. Wong, Appl. Catal. B **192**, 35 (2016)
37. Y. Lv, W. Yao, R. Zong, Y. Zhu, Sci. Rep. **6**, 19347 (2016)
38. Aİ. Vaizoğullar, J. Electron. Mater. **47**, 6751 (2018)
39. P. Intaphong, A. Phuruangrat, S. Thongtem, T. Thongtem, Mater. Lett. **213**, 88 (2018)
40. A. Phuruangrat, P. Dumrongrojthanath, B. Kuntalue, S. Thongtem, T. Thongtem, Mater. Lett. **196**, 256 (2017)
41. D. Zhang, H. Liu, C. Su, H. Li, Y. Geng, Sep. Purif. Technol. **218**, 1 (2019)
42. D. Wang, L. Guo, Y. Zhen, L. Yue, G. Xue, F. Fu, J. Mater. Chem. A **2**(30), 11716 (2014)
43. J. Liu, F. Xie, R. Li, T. Li, Z. Jia, Y. Wang, Y. Wang, X. Zhang, C. Fan, Mater. Sci. Semicond. Process. **97**, 1 (2019)
44. T. Liu, L. Wang, X. Lu, J. Fan, X. Cai, B. Gao, R. Miao, J. Wang, Y. Lv, RSC Adv. **7**(20), 12292 (2017)
45. K. Yu, S. Yang, H. He, C. Sun, C. Gu, Y. Ju, J. Phys. Chem. A **113**(37), 10024 (2009)
46. J. Luan, P. Huang, Materials **11**(4), 491 (2018)